Near Magnetic Field Assessment and Reduction for Magnetic Inductors With Magnetic Moment Analysis

Huan Zhang and Shuo Wang, *Fellow, IEEE*

Abstract—This article develops magnetic dipole moment models based on Maxwell's equations for inductor's near magnetic field evaluation and reduction in power electronics systems. In the developed model, the near magnetic field source of an inductor is composed of the magnetic dipole moments from the winding and the air gaps. The superposition of the magnetic dipole moments determines the near magnetic field. The developed model can be easily applied to inductors with different winding and air gap configurations, such as those with lumped or distributed air gaps, for near magnetic field assessment and reduction. Simulations and experiments are conducted to validate the developed theory.

Index Terms—Dipole, electromagnetic interference, inductors, magnetic moments, near magnetic field, transformers.

Nomenclature

J	Current density vector $[\mathbf{A}/\mathbf{m}^2]$.
M	Magnetization vector $[\mathbf{A}/\mathbf{m}]$.
B	Magnetic flux density vector $[\mathbf{T}]$.
H	Magnetic field intensity vector $[\mathbf{A}/\mathbf{m}]$.
J_b	Bound current density $[\mathbf{A}/\mathbf{m}^2]$.
H_{Jdip}	Dipole component of H_J $[\mathbf{A}/\mathbf{m}]$.
H_{Mdip}	Dipole component of H_M $[\mathbf{A}/\mathbf{m}]$.
A_J	Magnetic vector potential generated by J $[\mathbf{V} \cdot \mathbf{s}/\mathbf{m}]$.
A_{Jdip}	Dipole component of A_J $[\mathbf{V} \cdot \mathbf{s}/\mathbf{m}]$.
φ_M	Magnetic scalar potential generated by M $[\mathbf{A}]$.
φ_{Mdip}	Dipole component of φ_M $[\mathbf{A}]$.
m_J	Dipole moment generated by J $[\mathbf{A} \cdot \mathbf{m}^2]$.
m_M	Dipole moment generated by M $[\mathbf{A} \cdot \mathbf{m}^2]$.

I. Introduction

ELECTROMAGNETIC interference (EMI) has become a big concern in high switching frequency and high power density power electronics design [1]–[5]. In high power density design, the EMI caused by near field couplings is a headache issue [3], [18], [19]. One of the near-field sources is magnetic inductors. Inductors especially those carrying high ripple current generate not only the time-varying magnetic field inside the

magnetic cores but also the time-varying leakage magnetic field in the space. The leakage magnetic field can couple to other noise-sensitive components or circuits and compromise their functionalities. For example, the inductor of a boost power factor correction converter [18], [19], [24] or the resonant inductor of an LLC resonant converter [20] carries a high ripple current, so the leakage near the magnetic field from these inductors can compromise the performance of EMI filters or control circuits nearby. In high power density design, because of the small distance between components, EMI issues due to near field coupling are especially important. The mutual couplings between components within an EMI filter have been analyzed in considerable works [2], [6], [10]–[17]. An EMI filter with a good component layout has been proved to have good performance [2], [6], [14]–[17]. The analysis and reduction of the near magnetic field from toroidal inductors were presented in [3], [19], and [25]. The near magnetic field analysis is usually based on magnetic flux and reluctance. A stacked common-mode (CM) inductor structure is proposed in [3] to reduce the leakage near magnetic field due to DM currents and achieve the immunity to external magnetic field. Twisted winding structures are investigated in [19], [24], [25] to reduce near magnetic field generated from inductors. This article will develop magnetic dipole moment [19], [20] theory for inductors. The developed theory will be applied to the analysis and reduction of near magnetic field of U-core inductors with PCB windings, which are widely used in high power density design. The effectiveness of the developed theory and technique in this article has been validated in industry products.

In power electronics applications, for the inductor cores using high permeability magnetic materials, such as ferrite, air gaps are introduced to store energy and avoid saturation. Sometimes, an air gap is practically unavoidable because there is always a tiny gap between the two magnetic core parts. For example, there are always tiny air gaps between the two magnetic parts of EE, EI, UI, and UU cores. It will be analyzed and shown in this article that, without a careful design, these inductors can lead to significant near magnetic fields due to these air gaps.

The calculation of leakage magnetic field distribution for an inductor with a magnetic core can be very complicated. The boundary conditions for solving Maxwell's equations are closely related to the geometry of the core. In most cases, the calculation cannot be simplified pleasingly using the transformation of coordinate systems. Therefore, an approximation model needs to be developed to simplify the calculation. Zhang *et al.* [20], [21] use magnetic equivalent circuits to investigate the near magnetic field emission of inductors with different winding and air gap configurations. These works successfully developed

several inductor structures with reduced near magnetic field emission. However, as a classical inductor analysis and design technique, the magnetic equivalent circuit has its limitations when used for leakage magnetic field analysis. One difficulty is to determine the number and locations of the magnetic circuit branches used for modeling the leakage flux loops. In theory, these circuit branches should start and end at the magnetic cores whose reluctance are much smaller than those of the air gaps. As the number of air gaps and windings increases, the model becomes very complicated and so does the analysis. Also, for each magnetic circuit branch, it is impossible to determine the equivalent magnetic reluctance due to the uncertainty of the leakage flux propagation paths in the space. As a result, although the technique can provide some insights on the generation of leakage flux from simple inductor structures, it lacks the ability for an in-depth assessment and design, especially for those complicated inductor structures with multiple windings and multiple or distributed air gaps.

To overcome these limitations, this article proposes a theory to evaluate and reduce the near magnetic field of inductors based on magnetic moments. Employing dipole models for field analysis has been widely used [27]–[31] for printed circuit boards and other electronic devices. However, most existing works did not investigate the effect of magnetic materials, and the dipole models are derived based on measurement. For example, an equivalent set of elemental dipoles are derived based on data scanning in [28]–[31]. How to directly derive the model, simplify the analysis, and have a deep understanding of the field when magnetic materials are presented have been seldom talked about. In this article, both windings and air gaps are modeled as magnetic moments for near magnetic field analysis. In a nonoptimized inductor design, the magnetic moments mostly have the same direction that results in a strong leakage near the magnetic field; with the developed theory, the inductor design can be optimized so the magnetic moments can cancel each other, which leads to a greatly reduced the near magnetic field. The basic principle of the proposed theory is introduced in Section II. In Section III, some inductor winding and air gap structures are analyzed using the proposed theory and validated with finite element simulations. In Section IV, inductor prototypes are developed using UU cores to experimentally validate the proposed theory.

II. MAGNETIC MOMENT THEORY FOR INDUCTORS

A. Magnetic Field of an Inductor

In power electronics applications, the wavelength λ of the electromagnetic wave in the concerned EMI frequency range (for example, $< 30\text{MHz}$) in the free space is much larger than the dimensions of the inductors. In the space significantly closer than $\lambda/2\pi$ to the inductor, stationary field theory can be applied to analyze the near magnetic field without sacrificing the accuracy. In stationary field theory, for a magnetic inductor in Fig. 1, if μ_0 is the permeability of free space, when inductor winding carries a free current I with current density $\mathbf{J}$, the magnetic field intensity $\mathbf{H}$, the magnetic flux density $\mathbf{B}$, the bound current density $\mathbf{J_b}$, and the magnetization $\mathbf{M}$ always meet

$$\nabla \times \mathbf{H} = \mathbf{J} \tag{1}$$

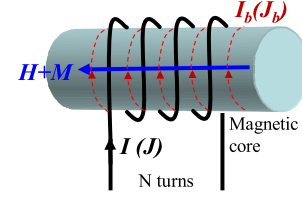$$\nabla \times \mathbf{M} = \mathbf{J_b} \tag{2}$$

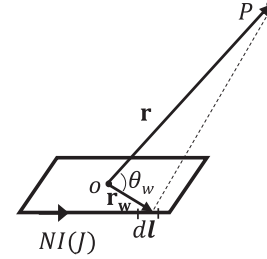Fig. 1. Magnetic inductor with N-turn winding carrying current I.

Fig. 2. Magnetic vector potential of a winding carrying current I.

$$\nabla \times (\mathbf{H} + \mathbf{M}) = \mathbf{J} + \mathbf{J_b} \tag{3}$$

$$\mathbf{B} = \mu_0(\mathbf{H} + \mathbf{M}) \tag{4}$$

$$\nabla \cdot \mathbf{B} = 0 \tag{5}$$

$$\nabla \cdot \mathbf{J_b} = 0 \tag{6}$$

$$\nabla \cdot \mathbf{J} = 0. \tag{7}$$

Based on electromagnetic theory, $\mathbf{J_b}$ is on the surface of the core; $\mathbf{M}$ is not zero inside the core but zero outside the core. The magnetization $\mathbf{M}$ is assumed to be uniform in the analysis.

Due to the linearity of Maxwell's equations, at any time, the magnetic field of an inductor is generated by two sources: the current density $\mathbf{J}$ of the windings and the bound current density $\mathbf{J_b}$. Although $\mathbf{J_b}$ is a function of $\mathbf{J}$, in magnetostatics, both are nearly constant during a short time interval and it is possible to treat them as independent. This enables us to analyze the fields generated by the two sources independently.

B. Magnetic Dipole Moment Generated by J in Windings

If an N-turn winding carries current I with current density $\mathbf{J}$, at the point $\boldsymbol{P}$ in the free space, based on electromagnetic theory, the magnetic flux density $\mathbf{B}$ generated by I can be calculated from magnetic vector potential $\mathbf{A}_J$ and it meets

$$\nabla \times \mathbf{A}_J = \mu_0 \mathbf{H}. \tag{8}$$

In Fig. 2, the N-turn winding carrying current I is simplified as a one-turn flat winding carrying current NI. Based on the Biot Savart Law, since the total MMFs of one equivalent turn and the N-turn winding are equal, when $r >> r_w$, the magnetic field generated by the one turn and N-turn windings are equal. The origin O is located within the winding. $\boldsymbol{r}$ is the position vector pointing from the origin O to the concerned point $\boldsymbol{P}$. $d\boldsymbol{l}$ is the infinitesimal displacement vector of the winding. $\boldsymbol{r_w}$ is a vector pointing from the origin O to $d\boldsymbol{l}$. θ_w is the angle between $\boldsymbol{r}$ and $\boldsymbol{r_w}$. With (1), (8), and Fig. 2, $\mathbf{A}_J$ can be solved and expressed in (9) in terms of Legendre polynomials $P_n(cos\theta_w)$ if $r >> r_w$
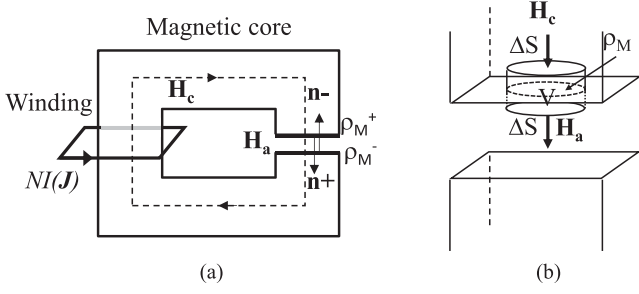
Fig. 3. (a) A UU core inductor with an air gap. (b) Magnetic surface charge ρ_M.

[22]

$$\mathbf{A}_J(\mathbf{r}) = \frac{\mu_0 NI}{4\pi} \sum_{n=0}^{\infty} \frac{1}{r^{n+1}} \oint (r_w)^n P_n(\cos\theta_w) dl \quad (9)$$

where the integration is a line integral along the winding turn. The condition $r \gg r_w$ does not invalidate the near field assumption as long as r is much smaller than the wavelength of the concerned frequencies.

Equation (9) can be expanded to the following:

$$\mathbf{A}_J(\mathbf{r}) = \frac{\mu_0 NI}{4\pi} \left[\frac{1}{r} \oint dl + \frac{1}{r^2} \oint r_w \cos\theta_w dl \right.$$
$$\left. + \frac{1}{r^3} \oint (r_w)^2 \left(\frac{3}{2}\cos^2\theta_w - \frac{1}{2} \right) dl + \ldots \right]. \quad (10)$$

In (10), the 1st term (monopole term) is zero. The 2nd term (dipole term) is dominant and a magnetic dipole moment $\mathbf{m}_J$ can be defined in (11), then (10) can be reduced to (12)

$$\mathbf{m}_J = NI \int d\mathbf{a} = NIA_W\hat{\mathbf{a}} \quad (11)$$

$$\mathbf{A}_{Jdip}(\mathbf{r}) = \frac{\mu_0 NI}{4\pi r^2} \oint r_w \cos\theta_w dl = \frac{\mu_0}{4\pi} \frac{\mathbf{m}_J \times \hat{\mathbf{r}}}{r^2}. \quad (12)$$

In (11) and (12), $\mathbf{a}$ is the vector area of the current loop with the direction assigned by the right-hand rule. It is equal to $A_W\hat{\mathbf{a}}$, where A_W is winding loop area and $\hat{\mathbf{a}}$ is the unit vector of $\mathbf{a}$. $\hat{\mathbf{r}}$ is the unit vector of $\mathbf{r}$, and $\mathbf{A}_{Jdip}(\mathbf{r})$ is the magnetic vector potential $\mathbf{A}_J$ in terms of the dipole term.

C. Magnetic Dipole Moment Due to $\mathbf{J}_b$

The UU core inductor in Fig. 3(a) has an N-turn winding carrying total current NI on the left leg and an air gap on the right leg. $\mathbf{H_c}$ and $\mathbf{H_a}$ are the magnetic field intensity in the core and air gap, respectively.

The magnetic flux density generated by surface bound current $\mathbf{J_b}$ can be analyzed with the help of the magnetic scale potential. Inside and outside of the core, $\mathbf{J_b}$ is zero, based on (2), $\mathbf{M}$ can be expressed as the negative gradient of a scalar φ_M because $\nabla \times (-\nabla\varphi_M) = 0$

$$\mathbf{M} = -\nabla\varphi_M. \quad (13)$$

From (4), (5), and (13)

$$\nabla^2\varphi_M = \nabla \cdot \mathbf{H} = -\nabla \cdot \mathbf{M} = \delta_M. \quad (14)$$

δ_M is magnetic charge density and (14) is Poisson's equation in the magnetostatic field. It is the same as Poisson's equation in the electrostatic field when the charge density δ_M is given. Therefore, the magnetostatic problem is mathematically equivalent to an electrostatic problem.

Because $\mathbf{M}$ is zero outside of the core and is assumed to be uniform inside the core, from (14), except at the surfaces of the air gap, δ_M is zero inside and outside the core. In Fig. 3(b), at the upper surface of the air gap, the effective magnetic surface charge density is ρ_M. Applying the Gauss Law to a Gaussian pillbox with an upper and lower surface area ΔS and a volume V straddling on the upper surface of the air gap, (15) can be derived

$$\mathbf{n} \cdot (\mathbf{H}_a - \mathbf{H}_c)\,\Delta S = \rho_M \Delta S + \frac{1}{2}\left(\delta_{Mc} + \delta_{Ma}\right)V. \quad (15)$$

In (15), $\mathbf{n}$ is the positive unit vector normal to the upper surface. The magnetic charge densities δ_{Mc} and δ_{Ma} inside the core and inside the air gap are zero, so

$$\rho_M = \mathbf{n} \cdot (\mathbf{H}_a - \mathbf{H}_c) \quad (16)$$

Equation (16) indicates that ρ_M is determined by the difference of magnetic field intensity $\mathbf{H}_a$ and $\mathbf{H}_c$ in the normal direction of the surface. Based on (16) and Fig. 3, because $\mathbf{H}$ flows from the upper surface to the lower surface, and $\mathbf{H}_a$ is much larger than $\mathbf{H}_c$ in magnitude, the magnetic surface charge density is positive $\rho_M{}^+$ for upper surface but negative $\rho_M{}^-$ for the lower surface as $\mathbf{n}$ is in the same direction as $\mathbf{H}_a - \mathbf{H}_c$ on the upper surface but in the opposite direction to $\mathbf{H}_a - \mathbf{H}_c$ on the lower surface. While the magnitude of $\mathbf{H}$ normal to all other surfaces of the core is much smaller than that in the air gap, so based on (16), the magnetic surface charge density on other surfaces is ignorable.

Since the magnitude of $\mathbf{H}_a$ is much larger than $\mathbf{H}_c$ in the air gap region, the effective magnetic surface charge density $\rho_M{}^+$ and $\rho_M{}^-$ can be calculated from (17) based on Ampere's law

$$\rho_M^{\pm} \approx (\mathbf{n}\pm) \cdot \mathbf{H}_a \approx \pm NI/l_g \quad (17)$$

where $\mathbf{n}\pm$ represent the unit norm vector for upper or lower surfaces of the air gap as in Fig. 3(a); l_g is the air gap length.

If the origin of the coordinate is located in the center of the air gap, and the concerned point P is located in the free space outside of the core. $\mathbf{r}_a$ is a vector pointing from the origin O to an infinitesimal area da_c on either surface of the air gap.

With the boundary condition in (17), (14) can be solved as

$$\varphi_M(\mathbf{r}) = \frac{1}{4\pi} \int \rho_M(\mathbf{r_a}) \frac{1}{\mathbf{r} - \mathbf{r_a}} da_c \quad (18)$$

where $\varphi_M(\mathbf{r})$ is the φ_M at point P due to $\rho_M{}^{\pm}$. $\rho_M(\mathbf{r_a})$ includes both $\rho_M{}^+$ on the upper surface and $\rho_M{}^-$ on the lower surface. The integrand can also be expanded in terms of Legendre polynomials

$$\varphi_M(\mathbf{r}) = \frac{1}{4\pi}\left[\frac{1}{r}\int \rho_M(\mathbf{r_a})da_c + \frac{1}{r^2}\int r_a\cos\theta_a\rho_M(\mathbf{r_a})da_c \right.$$
$$\left. + \frac{1}{r^3}\int (r_a)^2\left(\frac{3}{2}\cos^2\theta_a - \frac{1}{2}\right)\rho_M(\mathbf{r_a})da_c + \ldots \right].$$
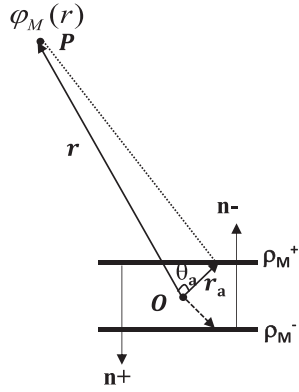$$(19)$$

Fig. 4. φ_M due to equivalent magnetic surface charge on the upper and lower surfaces of the air gap.

The 1st (monopole) term is zero for this case since the total magnetic charge on the two surfaces of the air gap is always zero as shown in (17). Since $r \gg r_a$, the 2nd (dipole) term dominates and a magnetic dipole moment $\mathbf{m}_M$ can be defined in (20) so (19) can be reduced to (21)

$$\mathbf{m}_M = \int \mathbf{r_a}\rho_M(\mathbf{r_a})da_c \tag{20}$$

$$\varphi_{Mdip}(\mathbf{r}) = \frac{1}{4\pi r^2}\int r_a\cos\theta_a\rho_M(\mathbf{r_a})da_c = \frac{1}{4\pi r^2}\hat{\mathbf{r}}\cdot\mathbf{m}_M \tag{21}$$

where $\varphi_{Mdip}(\mathbf{r})$ is the magnetic scalar potential φ_M in terms of the dipole term.

If there is only one air gap, from Fig. 4, (17) and (20)

$$\mathbf{m}_M = NIA_C\hat{\mathbf{d}} \tag{22}$$

where A_C is the equivalent cross-sectional area of the air gap. Due to the fringing effects, it could be a little bit larger than the core cross-sectional area. $\hat{\mathbf{d}}$ is a unit vector with the direction assigned by the polarities of the magnetic surface charges at the air gap (pointing from negative charge to positive charge).

If there are k air gaps in Fig. 3, there are k dipole moments $\mathbf{m}_{Mi}$, so the integration in (20) becomes

$$\mathbf{m}_M = \sum_{i=1}^{k}\mathbf{m}_{Mi} = |\rho_M|\,A_C\sum_{i=1}^{k}(\mathbf{r}_{ai+} - \mathbf{r}_{ai-})$$

$$= \frac{NIA_C}{\sum_{i=1}^{k}l_{gi}}\sum_{i=1}^{k}(\mathbf{r}_{ai+} - \mathbf{r}_{ai-}) \tag{23}$$

where $\boldsymbol{r}_{ai+}$ and $\boldsymbol{r}_{ai-}$ are position vectors of the positive and negative magnetic surface charges of the ith air gap, which are pointing from the origin to the centers of the positive and negative charged surfaces, respectively. $|\boldsymbol{r}_{ai+}-\boldsymbol{r}_{ai-}|$ is equal to the length l_{gi} of the ith air gap. The total magnitude of all dipole moments formed by the air gaps is always NIA_C, which is close to but smaller than NIA_W because usually $A_W > A_C$. The magnitude of the dipole moments for each air gap is proportional to the length of that air gap.
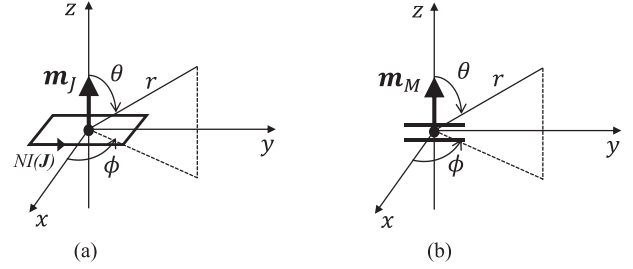

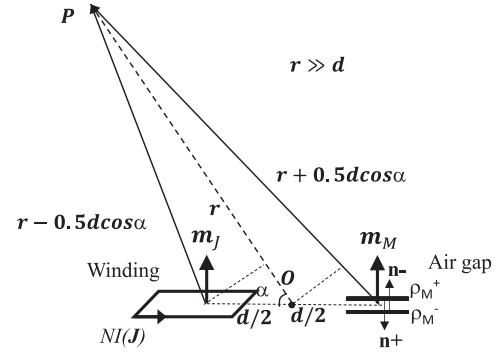Fig. 5. (a) Winding and (b) air gap in a spherical coordinate.

Fig. 6. Near magnetic field due to the winding and air gap.

D. Magnetic Field Generated by the Windings and Air Gaps

In a spherical coordinate in Fig. 5(a), (12) is rewritten as

$$\mathbf{A}_{Jdip}(r,\theta) = \frac{\mu_0 m\sin\theta}{4\pi r^2}\hat{\phi}. \tag{24}$$

Substituting (24) into (8), the magnetic field $\mathbf{H}_{Jdip}(\boldsymbol{r},\,\theta)$ can be calculated as

$$\mathbf{H}_{Jdip}(r,\theta) = \frac{m}{4\pi r^3}\left(2\cos\theta\hat{\mathbf{r}} + \sin\theta\hat{\theta}\right)$$

$$= \frac{NIA_W}{4\pi r^3}\left(2\cos\theta\hat{\mathbf{r}} + \sin\theta\hat{\theta}\right). \tag{25}$$

Similarly, in Fig. 5(b), (21) can be rewritten as

$$\varphi_{Mdip}(r,\theta) = \frac{m\cos\theta}{4\pi r^2}. \tag{26}$$

Substituting (26) into (14) and the magnetic field $\mathbf{H}_{Mdip}(\boldsymbol{r},\theta)$ can be calculated

$$\mathbf{H}_{Mdip}(r,\theta) = \frac{m}{4\pi r^3}\left(2\cos\theta\hat{\mathbf{r}} + \sin\theta\hat{\theta}\right)$$

$$= \frac{NIA_C}{4\pi r^3}\left(2\cos\theta\hat{\mathbf{r}} + \sin\theta\hat{\theta}\right). \tag{27}$$

From (25) and (27), the magnetic fields can be generated by different sources. The magnetic field at point $\mathbf{P}$ generated by the winding and air gap is superposed in the space in Fig. 6. The distance between the winding and the air gap is d, and the distance between the center O of d and $\mathbf{P}$ is r. It is assumed that $r \gg d$, and the angle between r and d is α, then the distance between the winding and P is around $r-0.5d\cos\alpha$ and the distance between the air gap and P is around $r+0.5d\cos\alpha$. If the average
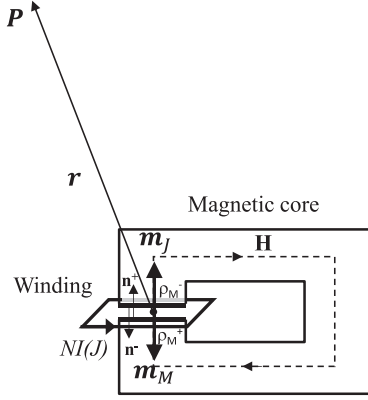
Fig. 7. Near magnetic field when the winding and air gap are on the same leg.

Fig. 8. Inductor structure with good near magnetic field cancellation.

of A_W and A_C is A, $A_W = A + \Delta A$ and $A_C = A - \Delta A$, where ΔA is the difference between A and A_W or A_C. The superposed magnetic field $\mathbf{H}(r,\theta)$ is approximately equal to

$$
\begin{aligned}
\mathbf{H}(r, \theta) &= \mathbf{H}_{Jdip}(r, \theta) + \mathbf{H}_{Mdip}(r, \theta) \\
&\approx \frac{NI}{4\pi}\left(2\cos\theta\hat{\mathbf{r}} + \sin\theta\hat{\theta}\right) \\
&\quad \times \left[\frac{A + \Delta A}{(r - 0.5d\cos\alpha)^3} + \frac{A - \Delta A}{(r + 0.5d\cos\alpha)^3}\right] \\
&\approx \frac{NI}{4\pi}\left(2\cos\theta\hat{\mathbf{r}} + \sin\theta\hat{\theta}\right)\left(\frac{2A}{r^3}\right).
\end{aligned}
\tag{28}
$$

(28) shows that because $\mathbf{m_J}$ and $\mathbf{m_M}$ have the same direction, the superposed magnetic field is around twice the individual magnetic field generated by the winding or air gap respectively. This indicates that the inductor structure in Fig. 3 has a high near a magnetic field. The magnitude of the magnetic field decreases at -60 dB/dec as r increases. Here, the decade is for the distance, not frequencies.

If the air gap and the winding are on the same leg as in Fig. 7, based on (16), the magnetic surface charge density is positive $\rho_M{}^+$ for the lower surface but negative $\rho_M{}^-$ for the upper surface as $\mathbf{n}$ is in the same direction as $\mathbf{H}$ on the lower surface but opposite direction to $\mathbf{H}$ on the upper surface. The magnetic moments $\mathbf{m_J}$ and $\mathbf{m_M}$ have reverse directions. Therefore

$$
\begin{aligned}
\mathbf{H}(r, \theta) &= \mathbf{H}_{Jdip}(r, \theta) + \mathbf{H}_{Mdip}(r, \theta) \\
&\approx \frac{NI}{4\pi}\left(2\cos\theta\hat{\mathbf{r}} + \sin\theta\hat{\theta}\right) \\
&\quad \times \left[\frac{A + \Delta A}{(r - 0.5d\cos\alpha)^3} - \frac{A - \Delta A}{(r + 0.5d\cos\alpha)^3}\right] \\
&\approx \frac{NI}{4\pi}\left(2\cos\theta\hat{\mathbf{r}} + \sin\theta\hat{\theta}\right)\left[\frac{2\Delta A}{r^3} + \frac{3Ad\cos\alpha}{r^4}\right].
\end{aligned}
\tag{29}
$$

(29) shows that because $\mathbf{m_J}$ and $\mathbf{m_M}$ have reverse directions, most of the magnetic fields from the winding and air gap are canceled. The remaining magnetic field is contributed from the area difference ΔA and distance between the winding and the air gap. If the centers of the winding and the air gap overlap, $d = $
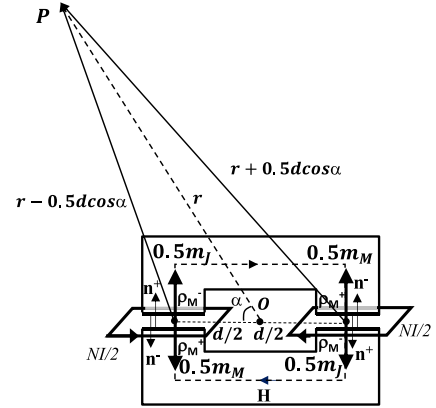
0. The remaining magnetic field will be solely contributed from ΔA and its magnitude decreases at -60 dB/dec as r increases. Based on the analysis above, the inductor in Fig. 7 has a much smaller near magnetic field than that in Fig. 3.

Because ΔA always exists between the winding and air gap in Fig. 7, the magnetic field generated by the winding and the air gap cannot be fully canceled. The inductor structure is proposed in Fig. 8 to further cancel the magnetic field. In Fig. 8, the winding is split into two winding halves on the two legs. At the same time, the air gap is also split into two halves on the two legs. The magnetic field (or $\mathbf{m_J}$) generated by the two winding halves, which are supposed to have an identical area, can cancel each other. Similarly, the magnetic field (or $\mathbf{m_M}$) generated by the two air gaps, which are supposed to have an identical area, can cancel each other. The remaining magnetic fields from the two winding halves and the two air gaps can further cancel each other and the final magnetic field is given by (30). In (30), A_W and A_C are the average areas of two winding halves and two air gap cross-sectional area respectively; ΔA_W is half of the winding loop area difference of two winding halves; ΔA_C is half of the difference of two air gap cross-sectional areas; ΔA_{WC} is the difference of the average areas of two air gap cross-sections and two winding halves.

$$
\begin{aligned}
\mathbf{H}(r, \theta) &= \mathbf{H}_{Jdip}(r, \theta) + \mathbf{H}_{Mdip}(r, \theta) \\
&\approx \frac{NI}{8\pi}\left(2\cos\theta\hat{\mathbf{r}} + \sin\theta\hat{\theta}\right) \\
&\quad \times \left[\frac{2}{r^3}(\Delta A_W - \Delta A_C) + \frac{3d\cos\alpha}{r^4}(A_W - A_C)\right] \\
&= \frac{NI}{8\pi}\left(2\cos\theta\hat{\mathbf{r}} + \sin\theta\hat{\theta}\right) \\
&\quad \times \left[\frac{2}{r^3}(\Delta A_W - \Delta A_C) + \frac{3d\Delta A_{WC}\cos\alpha}{r^4}\right].
\end{aligned}
\tag{30}
$$

In (30), ΔA_C and ΔA_W are usually zero, so the magnetic field will be determined by ΔA_{WC} and reduces at -80 dB/dec. Compared with (29), the magnitude of the magnetic field is further greatly reduced. If ΔA_{WC} is small enough, the quadrupole terms in (10) and (19) will become obvious and they reduce at
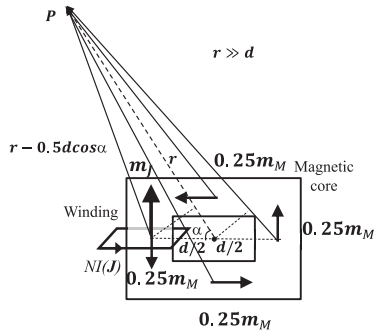
Fig. 9.   Inductor structure with a distributed air gap (low permeability) core.

-80 dB/dec too. So the near magnetic field will still reduce at -80 dB/dec.

For an inductor with distributed air gaps (with low permeability) in Fig. 9, the distributed magnetic moments $\mathbf{m_M}$ will have an inverse direction from the H field inside the core. The total distributed magnetic moments on each side of the core can be lumped based on (23) as in Fig. 9. In Fig. 9, the lumped magnetic moments on the top and bottom sides have the same magnitude but reverse directions, so they can greatly cancel each other. Similarly, the lumped magnetic moments on the left and right sides can greatly cancel each other too. The remaining magnetic field is due to the distance of the magnetic moments in each pair. The $\mathbf{m_J}$ is therefore not canceled and contributes to most of the magnetic field in space. The magnetic field is calculated in (31) and it decreases at -60 dB/dec as r increases

$$\mathbf{H}(r, \theta) = \mathbf{H}_{Jdip}(r, \theta) + \sum \mathbf{H}_{Mdip}(r, \theta)$$

$$\approx \frac{NI}{4\pi} \left(2\cos\theta\hat{\mathbf{r}} + \sin\theta\hat{\theta} \right) \left(\frac{A_W}{r^3} \right). \qquad (31)$$

From (28) and (31), the magnetic field of this structure will be around 6 dB lower than the structure in (28) and Fig. 3.

Similar to the structure in Fig. 8, the magnetic field in Fig. 9 can be greatly reduced by moving half winding to the right leg.

The magnetic moments of cores and air gaps represent the contributions of cores and air gaps to the near magnetic field. The analysis does not include the effect of the local core's low reluctance on the magnetic field in the region very close to the cores, but in the region $r >> r_d$, the analysis and conclusions still hold.

E. Summary

1) Both windings and air gaps generate magnetic fields in space. Both of them can be modeled as magnetic dipole moments: $\mathbf{m_J} = NIA_W$ and $\mathbf{m_M} = NIA_C$.
2) The direction of the winding magnetic dipole moment is the same as that of the magnetic field generated by itself, and the direction of the air-gap magnetic dipole moment is reverse to the direction of the magnetic field in the center of that air gap. The dipole moments with the same direction enhance the magnetic field and the dipole moments with reverse directions cancel the magnetic field.

3) The smaller the distance between the two reversely canceled magnetic moments is, and the smaller the cross-sectional area difference between two reversely canceled magnetic moments is, the better the cancellation is.
4) The magnitude of the magnetic field in the space generated by the winding or the air gap reduces at -60 dB/dec as the distance between the magnetic dipole moments and the concerned point in the space increases.
5) If the winding and the air gap are on the two side legs, their dipole moments have the same direction so the magnetic fields are added up and doubled. It reduces at -60 dB/dec as the distance between the core and the concerned point in the space increases.
6) If the winding and the air gap are on the same leg, their dipole moments have reverse directions so the magnetic field is greatly canceled and the remaining magnetic field is due to the difference of the cross-sectional areas between the winding and the air gap. The magnetic field reduces at -60 dB/dec as the distance between the core and the concerned point in the space increases.
7) If half of the winding and half of the air gap are located on the left leg and the other halves of the winding and air gap are located on the right leg, the magnetic dipole moments of two air gaps have reverse directions, so do the two winding halves. The winding magnetic moments on the two legs can cancel each other and the resulting magnetic field reduces at -80 dB/dec. The air gap magnetic moments on the two side legs can cancel each other and the resulting magnetic field reduces at -80 dB/dec. The magnetic field is significantly reduced but cannot be fully canceled due to the distance between the two halves. The greatly reduced magnetic field generated by the windings and the air gaps can further cancel each other to a very small level. The remaining magnetic field is due to the difference of cross-sectional areas between the windings and the air gaps. If the remaining magnetic field is small enough, the quadrupole terms in (10) and (19) will become obvious and they reduce at -80 dB/dec too, so the near magnetic field will still reduce at -80 dB/dec as r increases.
8) For a core with the distributed air gaps (low permeability), the distributed air gaps on each side leg can be represented using a lumped magnetic moment. Every two magnetic moments with the same magnitude but inverse directions are one cancellation pair. The magnetic fields generated from the two magnetic moments in each pair are canceled and the remaining magnetic field is due to the distance between two magnetic moments. The winding magnetic moment is not canceled so it dominates the magnetic field in space. The magnetic field reduces at -60 dB/dec as the distance between the core and the concerned point in the space increases. The magnetic field can be greatly reduced by moving the half winding to the other leg.

III. SIMULATION VERIFICATION

As analyzed in Section II, positions of the air gaps may have a great influence on the near magnetic field of the magnetic inductors. This section will validate the theory and analysis in

TABLE I
EXAMPLES OF INDUCTORS WITH -60 DB/DEC ($1/r^3$) NEAR MAGNETIC FIELD.

No.	No cancellation	P1	P2	P3	P4
Inductors and dipole moments					
Parameters	$N = 6$ $\mu_r = 3300$ $l_g = 0.5mm$ $L = 7.1\mu H$	$N = 6$ $\mu_r = 3300$ $l_{g1,2} = 0.25mm$ $L = 7.3\mu H$	$N = 6$ $\mu_r = 95$ $distributed\ airgaps$ $L = 7.0\mu H$	$N = 6$ $\mu_r = 3300$ $l_g = 0.5mm$ $L = 7.1\mu H$	$N = 6$ $\mu_r = 3300$ $l_{g1,2} = 0.25mm$ $L = 6.9\mu H$

TABLE II
EXAMPLES OF INDUCTORS WITH -80 DB/DEC ($1/r^4$) NEAR MAGNETIC FIELD

No.	F1	F2	F3	F4
Inductors and dipole moments				
Parameters	$N_{1,2} = 3$ $\mu_r = 3300$ $l_{g1,2} = 0.25mm$ $L = 7.4\ \mu H$	$N_{1,2} = 3$ $\mu_r = 3300$ $l_{g1,2} = 0.25mm$ $L = 6.5\ \mu H$	$N_{1,2} = 3$ $\mu_r = 3300$ $l_{g1,2,3,4} = 0.125mm$ $L = 6.4\ \mu H$	$N_{1,2} = 3$ $\mu_r = 3300$ $l_{g1,2,3,4} = 0.125mm$ $L = 8.5\ \mu H$

Section II. The near magnetic field of various inductor examples in Tables I and II will be simulated. Based on the analysis in Section II, the near magnetic fields of the inductor structures in Tables I and II have -60 dB/dec and -80 dB/dec reduction respectively as the distance r increases.

A. Inductor Structures With -60 dB/dec Reduction

In Table I, the baseline is the inductor without near magnetic field cancelation in Fig. 3. Its near magnetic field is characterized by (28). Inductor P1 has two air gaps with equal length located on two side legs. Based on the previous analysis, the magnitudes of their dipole moments are equal, but the directions are the opposite. So their near magnetic field is greatly canceled in space. On the other hand, the magnetic moment of the winding is not canceled, so the near magnetic field due to the winding will be dominant. Its near magnetic field is therefore characterized by (25) with -60 dB/dec reduction as the distance increases. Inductor P2 with distributed air gaps has been analyzed in Fig. 9 and (31). From (25), (28), and (31), P1 and P2 have almost the same near magnetic field; and the near magnetic field of the baseline inductor is twice (6 dB) higher than those of inductors P1 and P2. Inductor P3 has been analyzed in Fig. 7 and (29). Due to the cancellation of the magnetic dipole moments of the winding and the air gap, from (25), (29), and (31), comparing with P1 and P2, the near magnetic field of P3 is greatly reduced. Inductor P4 is similar to inductor P3 with the air gap split to two on the same leg as the winding. Because the centers of the two air gaps are not the same as the center of the winding, it is expected the near magnetic field cancellation will be slightly worse than P3. However, comparing with P3, P4 can reduce the
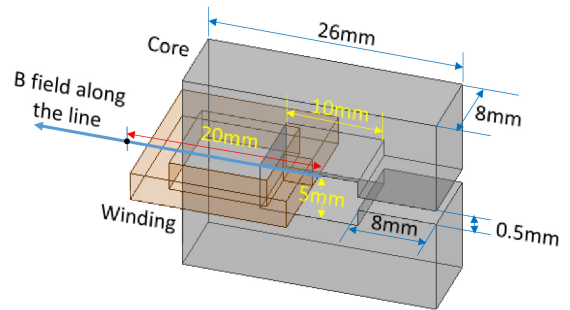

Fig. 10. Inductor dimensions in ANSYS Maxwell 3-D simulation.

winding eddy current power loss due to the fringing magnetic flux from the air gaps.

Fig. 10 shows the dimensions of the baseline inductor simulated in ANSYS Maxwell 3-D. The magnetic field was recorded along the line in Fig. 10 starting 20 mm distance to the center of the inductor. The core has a relative permeability of 3300. The air gap length is 0.5 mm. All other inductors have the same dimensions except the air gap length is reduced to half if there are two air gaps and the single winding's current is reduced to half if the winding is split into two halves.

Fig. 11 shows the simulated magnetic field magnitudes near the inductors at locations 20–200 mm away from the core center. It should be noted that the simulated fields are different in different directions due to the asymmetry of the inductor structures. In all simulations, $I = 1$ A and all other parameters are given in Table I. As predicted, all the simulated fields drop at the ratio of $1/r^3$, i.e., -60 dB/dec. As predicted, P1 and P2

Fig. 11. Simulated B field magnitudes for the inductors in Table I from 20 to 200 mm (log scale) away from the core geometry center.
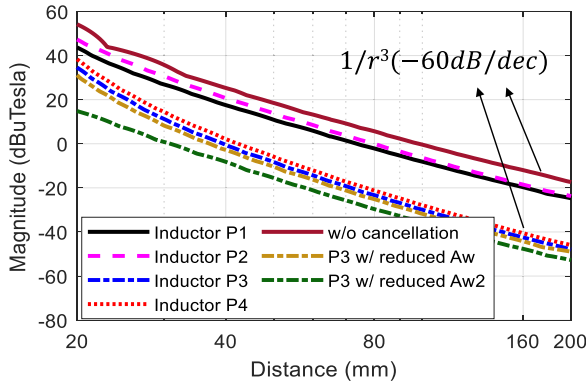

Fig. 12. Simulated B field magnitudes for the inductors in Table II from 20 to 200 mm (log scale) away from the core geometry center.

have similar performance and the magnetic field is around 6 dB lower than the baseline (w/o cancellation) inductor. P3 and P4 have similar performance but much better than P1 and P2. P3 is slightly better than P4 as predicted. Based on (29), reducing ΔA can help further reduce the near magnetic field. To validate this prediction, A_W is further reduced in Fig. 11. The equivalent loop area of the square shape winding is reduced from 169 to 144 mm^2 (reduced A_W) and 90.3 mm^2 (reduced A_{W2}), so it can be more close to A_C. The simulation shows that the near magnetic field can be further reduced by several dB. It should be noted that, in (10) and (19), when the dipole terms are greatly canceled, the high-order terms could become significant, so further reducing the near magnetic field will be limited.

The theory developed here has assumptions of $r >> r_w$, $r >> r_a$ and $r >> d$ in (10), (19), (28)–(31). In Fig. 11, in the distance from 20 to 40 mm, these assumptions are not well met so the slopes of the curves are not strictly -60 dB/dec. However, the magnitude sequence still agrees with the predicted because of the superposition of the magnetic moments.

B. Inductor Structure With -80 dB/dec Reduction

In Table II, the two air gaps on the top and bottom legs in inductor F1 can greatly cancel each other. Similarly, the two winding halves on the two legs can greatly cancel each other. As expected from Section II, the resulting magnetic fields of both cancellations reduce at -80 dB/dec. However, because the magnetic dipole moments of windings and air gaps are perpendicular, the remaining magnetic fields from the windings and air gaps cannot cancel each other, so the further reduction of the near magnetic field is limited. Inductor F2 has been analyzed in Fig. 8 and (30). The remaining magnetic field from both the windings and air gaps can further cancel each other, so it is expected that the near magnetic field will be much smaller than that of the inductor F1 and it reduces at -80 dB/dec. Inductor F3 is similar to inductor F2 with the air gap split into two on each leg. Because the centers of the two air gaps are not the same as the center of the winding, it is expected the near magnetic field cancellation will be slightly worse than F2 but much better than inductor F1. Comparing with F2, F3 may reduce the winding eddy current power loss due to the fringing magnetic flux from the air gaps.
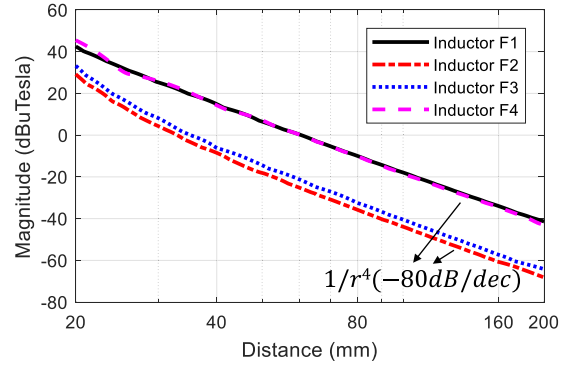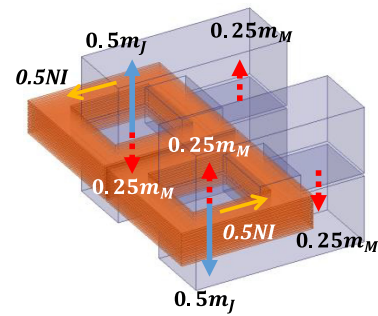

Fig. 13. Stacked-core inductor F5 and its dipole moment model with current directions indicated.

Inductor F4 is similar to inductor F1 with the air gap split into two on top and two on bottom legs. For the same reason, the magnetic dipole moments of the air gaps are perpendicular to those of the windings, the remaining magnetic field cannot further cancel each other. So the near magnetic field will be almost the same as that of the inductor F1.

Fig. 12 shows the simulated results in ANSYS Maxwell. As predicted, all simulated fields drop at the ratio of $1/r^4$, i.e., -80 dB/dec. Inductors F2 and F3 have much better performance than F1 and F4 as predicted. F2 is a little better than F3 as predicted too. In Fig. 12, in the distance from 20 to 40 mm, the assumptions of $r >> r_w$ and $r >> r_a$ in (10) and (19) are not well met, so the slopes of the curves are not strictly -80 dB/dec. Comparing the results in Figs. 11 and 12, the inductor structures with -80 dB/dec magnetic field reduction have a lower magnetic field than the inductor structures with -60 dB/dec magnetic field reduction as the distance increases although they are close when the distance is small.

Other inductor structures [3], [20] can be inspired by the same principle of dipole moment cancellation. A stacked-core inductor (F5) with air gaps on four legs and the windings on two left legs is shown in Fig. 13. The structure equivalently has two inductors in series and each inductor has half inductance. The air gap magnetic moments of each inductor cancel each other, and the remaining magnetic fields of the two inductors can further cancel each other. The two windings of the two inductors carry opposite currents so their magnetic dipole moments can cancel each other. Due to physical limitations, the two windings cannot
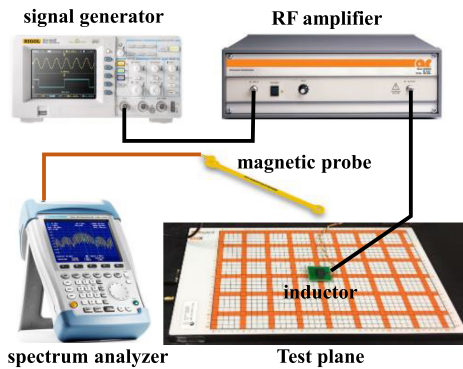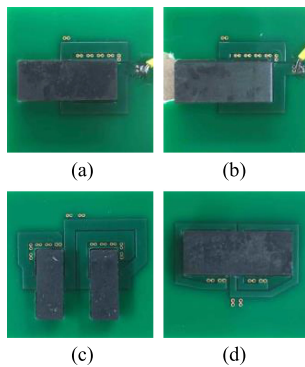
Fig. 14.   Near magnetic field test setup.

Fig. 15.   UU core planar inductor prototypes with (a) two identical air gaps and one winding (P1), (b) two air gaps and one winding on the same leg (P4), (c) two horizontally stacked cores (F5), and (d) two identical air gaps inside two windings (F2).

be very close, so the remaining near magnetic field is mostly due to the distance of the two windings and it reduces at −80 dB/dec.

IV. PROTOTYPE VERIFICATIONS

A signal generator RIGOL DS1052E, a Beehive Electronics 100-A EMC probe [26], a 25-W RF amplifier (model 25A250A) and a Rohde & Schwarz FSH4 spectrum analyzer were used in the experiment setup in Fig. 14. A 200-kHz sinusoidal voltage signal was generated by the signal generator. It was amplified by the RF amplifier and fed to the inductor. A current probe was used to monitor the input current at 1 A. The inductors were placed in the center of a coordinated board as shown in Fig. 14. The coordinated board has a $187.5\,\text{mm} \times 187.5\,\text{mm}$ area with $13 \times 13 = 169$ points on an equally spaced grid. The magnetic field probe was connected to the spectrum analyzer. The magnetic field flux density on a plane at 5 mm below the inductor is measured.

Four typical UU core planar inductors were prototyped as shown in Fig. 15. They are inductor P1 with two identical air gaps and one winding, inductor P4 with two air gaps and one winding on the same leg, inductor F5 with two horizontally stacked cores in Fig. 13 and inductor F2 with two identical air gaps inside two winding halves.

The parameters of the inductors P1, P4, and F2 are the same as those used in previous simulations. For inductor F5, it has two air gaps with equal length on each core. To maintain the
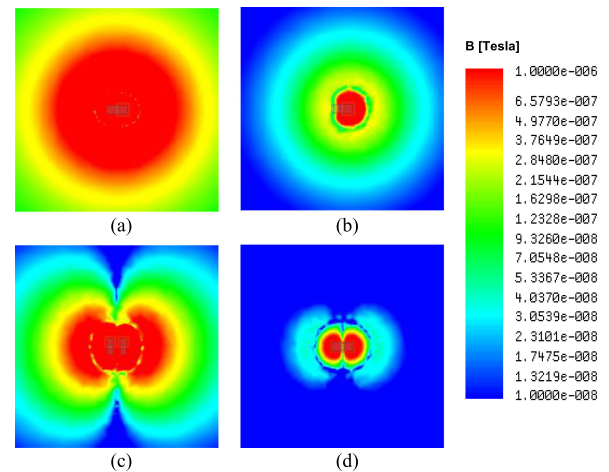
Fig. 16.   Simulated norm of magnetic flux density in z direction at a plane 5 mm below the inductors conducting 1 A current. (a) Inductor P1. (b) Inductor P4. (c) Inductor F5. (d) Inductor F2.

inductance for a fair comparison, the air gap lengths of F5 are $0.25\,\text{mm}$ and the core heights are the same as the other inductors. The cross-sectional area of each core is reduced by half. As for the number of turns, it is 6 for both windings.

The planar inductors have a winding made from a 12-layer PCB. In Fig. 15(a)–(c), each winding turn is composed of 2 PCB layers in parallel while in Fig. 15(d) each turn has 4 PCB layers in parallel. Therefore, the winding widths in Fig. 15(d) are reduced by half in the figures to maintain a similar winding cross-sectional area. The inductances of all inductors are adjusted during manufacturing to be around $6.5\,\mu\text{H}$.

The norm of z-component magnetic flux density (i.e., the magnetic flux perpendicular to the PCB) 5 mm below an inductor conducting 1 A current is simulated and measured. Z-component is selected for illustration since in many cases, Z-component magnetic flux plays a major role on the near field couplings to the nearby PCB traces, which is on the x–y plane, and the planar components on the PCB. In some cases, the y/z-component is also important but they follow the similar trend to that of the z-component when the distance increases so the results are not shown here. Fig. 16 shows the simulated norm of z-component magnetic flux densities.

Fig. 17 shows the corresponding experimental results. The magnetic field flux density color maps are on a logarithmic scale. The results in the two figures match very well. Same as the analytical results, the inductor F2 with two identical air gaps enclosed by two windings has the lowest near magnetic field emission of all as shown in the figures. The inductor P4 with two air gaps and one winding on the same leg and the inductor F5 with two horizontally stacked cores have lower near magnetic field emission than the single winding inductor P1 with two identical air gaps on two legs. In Figs. 16(c) and 17(c), the area close to the symmetric line of the two windings of inductor F5 with two stacked cores has a lower magnetic field flux density than other areas nearby. This is because, at the centerline of two opposite dipoles, the near magnetic field can get well canceled. The near magnetic field emission of inductor F5 can be further reduced if the two cores are closer that will be possible when spiral wire windings instead of PCB windings are used.
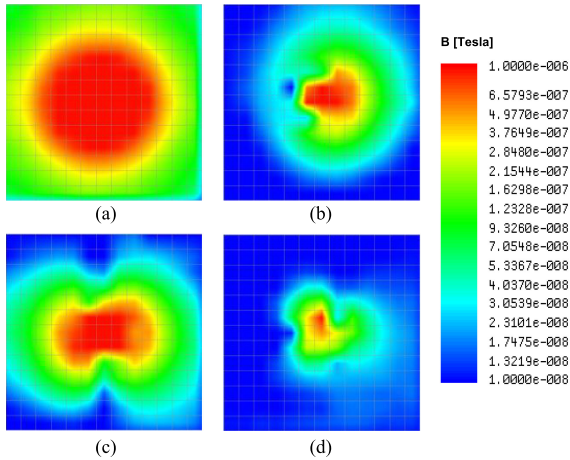
Fig. 17. Measured norm of magnetic flux density in z direction at a plane 5 mm below the inductors conducting 1 A current. (a) Inductor P1. (b) Inductor P4. (c) Inductor F5. (d) Inductor F2.

It should be mentioned some factors can cause the difference between the simulation and measurement. One factor is the winding layout. In the simulation, the winding is an ideal symmetrical one-turn winding. The windings on the prototypes are asymmetric since the vias and additional length have to be added to finish turn layout and make connection between turns. Its impact is mainly in the region very close to the inductor when high order components of the field are still substantial. When the distance to the inductor increases, the influence diminishes. This is especially true for the inductors (c) and (d) in Figs. 15–17, whose PCB winding layouts are more complex than those of (a) and (b). The second factor is the feeding wires connecting the inductor under test to the RF amplifier. For the measurements in Fig. 17, the feeding wires are all from the right side of the inductor. Since the feeding wires carry current, they make the nearby field stronger. The impact of the feeding wires can be easily identified when the field of the inductor is weak. In Fig. 17(a), the field is almost symmetrical and similar to the simulated in Fig. 16(a) when the field generated by the inductor is strong. In Fig. 17(b)–(d), the field strength on the right side of the inductor tends to be stronger than that on the left side due to the existence of feeding wires from the right side. Since the inductors in Fig. 17(c) and (d) generate a weaker field, the impact of the feeding wires is more significant. Nevertheless, the impacts of the two factors are relatively small and the theory proposed in this article still holds when $r \gg r_d$.

V. APPLYING TO OTHER MAGNETIC STRUCTURES

The developed theory can be applied to the analysis of the near magnetic field of other magnetic structures such as inductors with EE cores, toroidal cores, and other shape cores. It can also be applied to the near magnetic field analysis for transformers. Figs. 18 and 19 show the inductors with EE cores and toroidal cores.

In Fig. 18(a), the three magnetic moments from the winding and air gaps have the same direction, so their magnetic field will be enhanced and reduces at −60 dB/dec. It is the worst of the three. In Fig. 18(b), the magnetic moments of three air gaps cancel each other but the winding magnetic moment is not
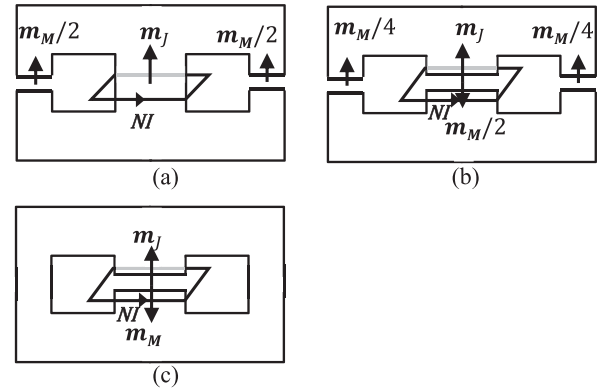

Fig. 18. EE core inductors with the winding on the center leg and the air gaps at different locations. (a) Two air gaps on the two side legs. (b) Three air gaps on all three legs. (c) One air gap on the center leg.
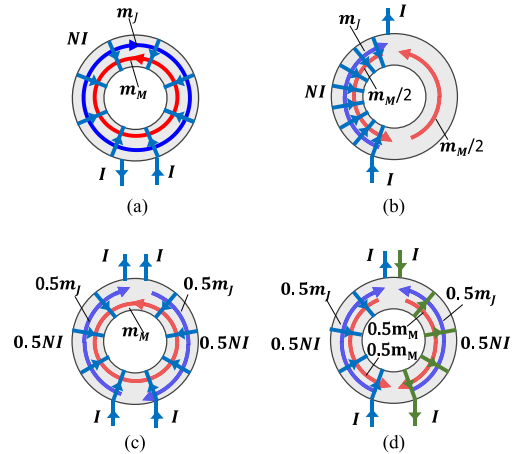

Fig. 19. Toroidal core inductors with different winding structures. (a) One evenly distributed winding. (b) One lumped winding. (c) CM inductor with a CM current excitation. (d) CM inductor with a DM current excitation.

canceled so its magnetic field is 6 dB lower than Fig. 18(a) and reduces at −60 dB/dec. In Fig. 18(c), the magnetic moments of the winding and air gap greatly cancel each other, so the magnetic field is the lowest. It reduces at −60 dB/dec.

In Fig. 19(a), a single-ended 360° winding structure has 360° distributed winding and air gap magnetic moments. Either one can cancel itself or cancel each other, so the near magnetic field is very small. On the other hand, the 360° equivalent winding current loop [25] instead will generate a dominant near a magnetic field. In Fig. 19(b), if the winding covers part of the toroidal core, the 360° distributed air gap magnetic moments of the core can cancel itself, but the winding magnetic moment does not, so the near magnetic field is higher than Fig. 19(a). In Fig. 19(c), for a balanced CM inductor winding structure with a CM current excitation, the magnetic moments of two windings can cancel each other, and the 360° distributed air gap magnetic moments of the core can cancel itself. The magnetic moments of windings and the 360° distributed air gap can also cancel each other, so its near magnetic field is similar to Fig. 19(a) and is very small [25]. In Fig. 19(d), for a CM inductor with a DM current excitation, the two winding magnetic moments have the same
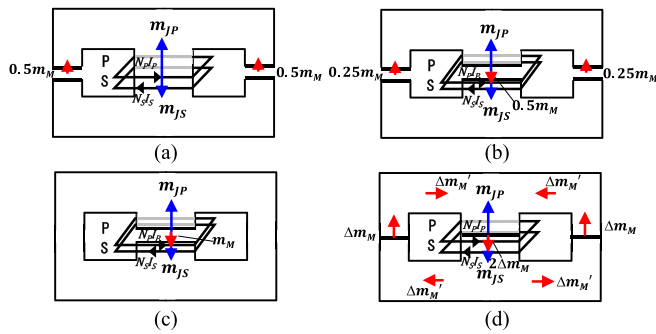
Fig. 20. EE core transformers with the windings on the center leg and the air gaps at different locations. Flyback transformers: (a) two air gaps are on the two side legs, (b) three air gaps are on all three legs, (c) one air gap is on the center leg; a conventional transformer: (d) with very small air gaps on three legs.

direction, so do the two distributed air gap magnetic moments. The winding and distributed air gap magnetic moments on each side can cancel each other, but the remaining magnetic field, which contributes to DM inductance, will be enhanced. It should be noted that due to the winding imperfections, a practical toroidal inductor structure may generate different fields than the theoretically predicted.

Fig. 20(a)–(c) shows a flyback transformer with EE cores and air gaps at different locations. Based on the operating principle of the flyback converters, the current ratio of the primary winding P and the secondary winding S is significantly different from the current ratio relationship of the conventional ideal transformer (equal to the inverse of the turn ratio). Therefore, the magnetic moments of the two windings are significantly unequal. Because of this, for the transformer in Fig. 20(a), the magnetic moments m_{JP} and m_{JS} of two windings N_P and N_S, which carry current I_P and I_S, cannot cancel each other. Furthermore, the magnetic moments, which is $0.5m_M$, of two air gaps have the same direction as the net magnetic moment of the windings in the center leg, therefore, they enhance each other. The near magnetic field is therefore high. In Fig. 20(b), the magnetic moment $0.5m_M$ of the central air gap cancels the magnetic moments of the air gaps on the two side legs, but the magnetic moments m_{JP} and m_{JS} of two windings are not canceled, so the near magnetic field is high but 6 dB smaller than Fig. 20(a). In Fig. 20(c), the magnetic moments m_{JP}, m_{JS}, and m_M of the windings and the air gap cancel each other, so the near magnetic field is the lowest. The near magnetic field of all of these transformers reduces at -60 dB/dec as the distance increases.

For conventional transformers, since the air gaps are very small, both the magnetic dipole moments of the undesired small air gaps and the distributed air gaps (even with high permeability) in the core should be considered. Fig. 20(d) shows the conventional transformers. The magnetic moments m_{JP} and m_{JS} of primary and secondary windings can be partially canceled as the magnetic moment due to the magnetizing current cannot be canceled. The magnetic moments of the three undesired air gaps can cancel each other and the distributed air gaps in the core can cancel each other. As a result, the winding magnetic moment due to the magnetizing currents contributes to most of the near magnetic field. It reduces at -60 dB/dec. Smaller magnetizing currents thus have lower near magnetic fields.

The developed theory can also be applied to three-phase inductors and transformers but due to the space limit, it will not be detailed here.

VI. CONCLUSION AND FUTURE WORK

To evaluate and reduce the near magnetic field of magnetic components, this article developed a theory for the near magnetic field analysis by employing magnetic dipole moment models. Based on the developed models, the near magnetic field performance of inductors with different winding and air gap configurations can be well estimated or optimized. Some typical inductor structures were analyzed, and their near magnetic field performance was evaluated. Based on the developed models, it can be determined that some magnetic structures have lower near magnetic field emissions than others. Some general principles are derived from the models. Inductor prototypes were built accordingly. Simulations and experimental results verified the proposed models and the analysis. The developed theory is applied to the near magnetic field analysis of other magnetic components including EE core inductors, toroidal core inductors, flyback transformers, and conventional transformers.

The developed dipole moment model is a good tool for the near magnetic field assessment and reduction in an inductor and transformer design. Although the complexity of accurate calculations becomes intimidating if the effect of the local low reluctance core (i.e., the related boundary condition) is considered. It has been proved in simulations, experiments, and the sponsored commercial products that the proposed theory is good enough for the evaluation and eduction of near magnetic field emission from magnetic components qualitatively. This article also pointed out that there is a tradeoff between the near magnetic field reduction and the winding power loss due to the fringing flux of the air gaps. The actual engineering design depends on the preferred optimization objects.

The near magnetic field assessment and reduction for three-phase inductors and transformers based on the magnetic moment theory developed here will be published later.

REFERENCES

[1] R. X. Lai, Y. Maillet, F. Wang, S. Wang, R. Burgos, and D. Boroyevich, "An integrated EMI choke for differential-mode and common-mode noise suppression," *IEEE Trans. Power Electron.,* vol. 25, no. 3, pp. 539–544, Mar. 2010.

[2] R. X. Wang, H. F. Blanchette, M. K. Mu, D. Boroyevich, and P. Mattavelli, "Influence of high-frequency near-field coupling between magnetic components on EMI filter design," *IEEE Trans. Power Electron.,* vol. 28, no. 10, pp. 4568–4579, Oct. 2013.

[3] Y. Chu, S. Wang, N. Zhang, and D. Fu, "A common mode inductor with external magnetic field immunity, low-magnetic field emission, and high-differential mode inductance," *IEEE Trans. Power Electron.,* vol. 30, no. 12, pp. 6684–6694, Dec. 2015.

[4] H. Zhang, S. Wang, Y. Li, Q. Wang, and D. Fu, "Two-capacitor transformer winding capacitance models for common-mode EMI noise analysis in isolated DC-DC converters," *IEEE Trans. Power Electron.,* vol. 32, no. 11, pp. 8458–8469, Nov. 2017.

[5] H. Zhang, L. Yang, S. Wang, and J. Puukko, "Common-mode EMI noise modeling and reduction with balance technique for three-level neutral point clamped topology," *IEEE Trans. Ind. Electron.,* vol. 64, no. 9, pp. 7563–7573, Sep. 2017.

[6] S. Wang, R. Chen, J. D. Van Wyk, F. C. Lee, and W. G. Odendaal, "Developing parasitic cancellation technologies to improve EMI filter performance for switching mode power supplies," *IEEE Trans. Electromagn. Compat.,* vol. 47, no. 4, pp. 921–929, Nov. 2005.

[7] T. C. Neugebauer and D. J. Perreault, "Filters with inductance cancellation using printed circuit board transformers," *IEEE Trans. Power Electron.,* vol. 19, no. 3, pp. 591–602, May 2004.

[8] R. G. Chen, J. D. van Wyk, S. Wang, and W. G. Odendaal, "Improving the characteristics of integrated EMI filters by embedded conductive layers," *IEEE Trans. Power Electron.,* vol. 20, no. 3, pp. 611–619, May 2005.

[9] S. Wang, F. C. Lee, and J. D. van Wyk, "Design of inductor winding capacitance cancellation for EMI suppression," *IEEE Trans. Power Electron.,* vol. 21, no. 6, pp. 1825–1832, Nov. 2006.

[10] S.-P. Weber, E. Hoene, S. Guttowski, J. John, and H. Reichl, "Predicting parasitics and inductive coupling in EMI-filters," in *Proc. 21st Annu. IEEE Appl. Power Electron. Conf. Expo.*, Apr. 2006, pp. 1157–1160.

[11] S. Wang, F. C. Lee, W. G. Odendaal, and J. D. van Wyk, "Improvement of EMI filter performance with parasitic coupling cancellation," *IEEE Trans. Power Electron.,* vol. 20, no. 5, pp. 1221–1228, Sep. 2005.

[12] S. Wang, F. C. Lee, D. Y. Chen, and W. G. Odendaal, "Effects of parasitic parameters on EMI filter performance," *IEEE Trans. Power Electron.,* vol. 19, no. 3, pp. 869–877, May 2004.

[13] L. Yang and S. Wang, "A compensation winding structure for balanced three-phase coupled inductor," in *Proc. Appl. Power Electron. Conf. Expo.*, Mar. 2017, pp. 868–875.

[14] M. Hartmann, H. Ertl, and J. W. Kolar, "EMI filter design for a 1 MHz, 10 kW three-phase/level PWM rectifier," *IEEE Trans. Power Electron.,* vol. 26, no. 4, pp. 1192–1204, Apr. 2011.

[15] T. De Oliveira, J.-L. Schanen, J.-M. Guichon, and L. Gerbaud, "Automatic layout optimization of an EMC filter," in *Proc. IEEE Energy Convers. Congr. Expo.*, Sep. 2010, pp. 2679–2685

[16] J. Aime, E. Clavel, J. Roudet, and P. Baudesson, "Determination of the layout influence on the effectiveness of a three-phase common mode filter by using equivalent circuits and PSpice," in *Proc. Int. Symp. Ind. Electron.*, 2008, pp. 1–6.

[17] C. Wei, F. Limin, C. Henlin, and Q. Zhaoming, "Near field coupling effects on conducted EMI in power converter," in *Proc. 37th IEEE Power Electron. Specialists Conf.*, Jun. 2006, pp. 1–6.

[18] H. L. Chen and Z. M. Qian, "Modeling and characterization of parasitic inductive coupling effects on differential-mode EMI performance of a boost converter," *IEEE Trans. Electromagn. Compat.,* vol. 53, no. 4, pp. 1072–1080, Nov. 2011.

[19] B. Zhang and S. Wang, "Analysis and reduction of the near magnetic field radiation from magnetic inductors," in *Proc. Appl. Power Electron. Conf. Expo.*, Mar. 2017, pp. 2494–2501.

[20] H. Zhang, S. Wang, and Q. Wang, "Winding and air gap configurations for power inductors to reduce near magnetic field emission," in *Proc. Energy Convers. Congr. Expo.*, Oct. 2017, pp. 903–910.

[21] H. Zhang, B. Zhang, and S. Wang, "Integrated common mode and differential mode inductors with low near magnetic field emission," in *Proc. Energy Convers. Congr. Expo.*, Oct. 2017, pp. 5375–5382.

[22] D. J. Griffiths, *Introduction to Electrodynamics*. Upper Saddle River, NJ, USA: Prentice Hall, 2005.

[23] M. Albach and A. Stadler, "The minimization of magnetic stray fields from toroids with air gaps," in *Proc. Int. Symp. Electromagn. Compat. (IEEE Cat. No.04CH37559)*, Aug. 2004, vol. 3, pp. 881–886.

[24] Y. Lai, S. Wang, and B. Zhang, "Investigation of magnetic field immunity and near magnetic field reduction for the inductors in high power density design," *IEEE Trans. Power Electron.,* vol. 34, no. 6, pp. 5340–5351, Jun. 2019.

[25] B. Zhang and S. Wang, "Analysis and reduction of the near magnetic field emission from toroidal inductors," *IEEE Trans. Power Electron.*, vol. 35, no. 6, pp. 6251–6268, Jun. 2020.

[26] 100 Ser. EMC Probes. Available: [Online]. Available: https://beehive-electronics.com/datasheets/100SeriesDatasheetCurrent.pdf

[27] K. Yamazaki and T. Kawamoto, "Simple estimation of equivalent magnetic dipole moment to characterize ELF magnetic fields generated by electric appliances incorporating harmonics," *IEEE Trans. Electromagn. Compat.*, vol. 43, no. 2, pp. 240–245, May 2001.

[28] D. W. P. Thomas, C. Obiekezie, and X. Tong, "Equivalent dipole models of electromagnetic emissions from near-field scanning," *IEEE Electromagn. Compat. Mag.*, vol. 4, no. 3, pp. 74–78, Jul.–Sep. 2015.

[29] L. Beghou, B. Liu, L. Pichon, and F. Costa, "Synthesis of equivalent 3-D models from near field measurements—Application to the EMC of power printed circuit boards," *IEEE Trans. Magn.*, vol. 45, no. 3, pp. 1650–1653, Mar. 2009.

[30] Z. Yu, J. A. Mix, S. Sajuyigbe, K. P. Slattery, and J. Fan, "An improved dipole-moment model based on near-field scanning for characterizing near-field coupling and far-field radiation from an iC," *IEEE Trans. Electromagn. Compat.*, vol. 55, no. 1, pp. 97–108, Feb. 2013.

[31] Y. Liu, B. Ravelo, and A. K. Jastrzebski, "Time-Domain magnetic dipole model of PCB near-field emission," *IEEE Trans. Electromagn. Compat.*, vol. 58, no. 5, pp. 1561–1569, Oct. 2016, doi: 10.1109/TEMC.2016.2578953.

Huan Zhang received the Ph.D. degree in electrical engineering from the University of Florida, Gainesville, FL, USA, in 2019.

He is currently a Sr. Power Electronics / EMC Design Engineer at Tesla Inc., where he is involved in EMC design and research for power electronics products made by Tesla Inc. He has authored or coauthored several journal and conference papers and holds four US patents. His current research interests include power electronics systems, EMI modeling and system simulation, EMI suppression for power electronic products, and magnetic components design.
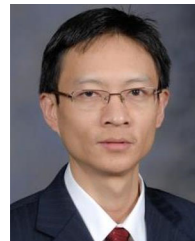
Shuo Wang (Fellow, IEEE) received the Ph.D. degree in electrical engineering from Virginia Tech, Blacksburg, VA, USA, in 2005.

He is currently a Full Professor with the Department of Electrical and Computer Engineering, University of Florida, Gainesville, FL, USA. He has authored or coauthored more than 200 IEEE journal and conference papers and holds around 30 pending/issued US/international patents.

Dr. Wang was the recipient of the Best Transaction Paper Award from the IEEE Power Electronics Society in 2006 and two William M. Portnoy Awards for the papers published in the IEEE Industry Applications Society in 2004 and 2012, respectively. In 2012, he was also the recipient of the prestigious National Science Foundation CAREER Award. He is an Associate Editor for the IEEE TRANSACTIONS ON INDUSTRY APPLICATIONS and IEEE TRANSACTIONS ON ELECTROMAGNETIC COMPATIBILITY. He is the Chair of Power Electronics EMI/EMC special committee of IEEE EMC Society and an instructor of IEEE Clayton Paul Global University. He was a Technical Program Co-Chair for the IEEE 2014 International Electric Vehicle Conference.